Science
AAAS

Supplementary Materials for

Where rivers jump course

Sam Brooke *et al*.

Corresponding author: Vamsi Ganti, vganti@ucsb.edu

Science **376**, 987 (2022)
DOI: 10.1126/science.abm1215

The PDF file includes:

Supplementary Text
Figs. S1 to S12
References

Other Supplementary Material for this manuscript includes the following:

Table S1
Movies S1 and S2

Text S1: Avulsion database

a. New avulsion events mapped using satellite imagery

We followed previous work to identify avulsions from the time series of satellite imagery (*31*, *38*). We located avulsion events on alluvial fans and deltas by manually examining planform change in rivers across the global coastlines, lakes, and mountain fronts. We focused on the lobe-scale avulsions, i.e., the largest-scale avulsion events that occur at the apex of fans and deltas that caused a permanent shift in the river course from the apex to the axial river or the shoreline. We did not consider intralobe avulsions and bifurcations at the river mouths in our study. The controls on the location where intralobe avulsions and bifurcations occur is different than lobe-scale avulsions, which set the size of fans and deltas. Thus, it is critical to assess avulsions using a time series of satellite imagery rather than static satellite images where avulsions can be conflated with bifurcations. The time between successive avulsions is inversely proportional to the in-channel sedimentation rates (*39*), which in turn is set by fluvial sediment supply (*40*). Avulsion timescales on the order of years to decades that facilitate the direct observation of avulsions in the satellite record, therefore, occur in the tropics and regions where steep, sediment-laden rivers could form deltas.

We identified avulsions using a combination of the global surface water change masks (*18*) and analysis of the time series of Landsat imagery. In most cases, avulsion locations were immediately apparent from surface water change masks (Fig. S1), showing clearly where previous channels had been abandoned in favor of a new channel feeding its new delta or fan lobe. We also downloaded and curated the full Landsat time series data for each candidate avulsion event, and turned these images into time-lapse animations (see videos S1 and S2 for delta and fan avulsion time-lapse examples), where each cloud-free image represented a single frame. We explored the available NASA/USGS Landsat archive (1972-2021) for cloud-free multispectral images, which included Landsat 1-4 MSS sensor data with ~60 m pixel resolution (up to 1984 C.E.) and Landsat 5-8 TM/ETM+/OLI ~30 m pixel resolution data (1984 C.E. onwards). The advantage of full time-lapse animations was the ability to discriminate between rapid yet continuous migration of river channels across the floodplains from avulsion events. Further, this method allowed us to distinguish lobe-scale avulsions from intralobe avulsions (where the flow rejoins the trunk channel at a downstream location) and bifurcations. To better

highlight changes in surface water, we employed the near-infrared (NIR) bands (Fig. S1) and indices such as the Normalized Difference Water Index (NDWI) when analyzing the Landsat imagery (Movie S2).

We used the aforementioned methodology to locate avulsions globally. For each avulsion event, we recorded the latitude and longitude of the avulsion site (Table S1), i.e., the location at which the river pathway diversion was initiated. In all cases, the avulsion location was stable during the relocation process. The mapping of avulsion sites was possible using the Landsat image taken closest to the avulsion event, with avulsion sites marked as a point on the channel centerline. The error of avulsion locations is hence half the width of the channel. To assess topographic changes at the avulsion sites, we extracted topographic swath profiles across the avulsion sites (see Text S2). For the delta avulsion sites, we estimated the avulsion length, L_A, which was defined as the streamwise distance from the avulsion site to the river mouth of the parent channel at the time the avulsion was initiated. For this computation, we chose the Landsat image that best captured the avulsion event and manually measured the streamwise distance between the avulsion site and river mouth in QGIS.

Finally, to mitigate selection bias, we worked as three separate teams to independently record the location and timing of avulsion events across the globe. In doing so, we were able to corroborate each avulsion site and confirm its validity as a lobe-scale avulsion event, and whether the exact timing could be determined from a thorough exploration of the Landsat imagery archive. In total, we identified 90 avulsion events in the satellite record of which 13 avulsion events were previously reported (*6*, *31*, *35*, *41*). The other 23 avulsion events in our global database were previously reported in the literature and pre-dated the satellite record.

b. Compilation of previously-reported historical river avulsions on fans and deltas

We augmented the new observations of avulsions with a compilation of previously-reported avulsions on fans and deltas. For the delta avulsions, we restricted our analysis to avulsion sites that were either mapped in satellite imagery or on historical maps, which allowed for an assessment of the avulsion length, L_A. In total, we compiled 36 previously-reported lobe-scale avulsions on fans and deltas (Table S1). The majority of these avulsions were from large, lowland delta systems. Our database included 6 avulsions mapped on the Sulengguole River delta using landsat imagery (*35*), 7 delta avulsions and 9 fan avulsions on the Huanghe (*9*, *13*),

which were located on historical maps (*42–44*), 8 avulsion sites mapped on large, lowland river deltas (*22*, *25*), 5 delta avulsion sites on the island of Madagascar located using satellite imagery (*31*), and the Kosi river avulsion of 2008 C. E (*6*). We analyzed all these previously-reported avulsions by computing the topographic changes associated with avulsions (Text S2) and the flood variability controls on avulsions (Text S4). We also excluded, to the best of our knowledge, the avulsions that were engineered, i.e., human-made flow diversions.

Text S2: Extraction of topographic swath profiles from global digital elevation models

Channel floodplain and adjacent topographic swath profiles were extracted from a combination of NASA's ~30 m spatial resolution Shuttle Radar Topography Mission (SRTM) and JAXA's ~30 m spatial resolution ALOS Global Digital Surface Model (AW3D30) elevation datasets (Fig. S2). The SRTM mission was conducted in February 2000 C.E., and the AW3D30 is a composite model of multiple ALOS stereo pairs taken between 2006 to 2011 C.E. We chose this combination of multiple observations of elevation for each site because it is likely to improve the signal-to-noise ratio, when compared to having a single capture in 2000 C.E. The SRTM data is prone to noise, especially at low elevations near the shoreline, due to radar backscatter anomalies from standing water and vegetation. The AW3D30 data, however, is less prone to error from standing body of water. We used a combination of elevation values from SRTM and AW3D30 products to a create a single channel-floodplain and topographic swath profile for each river to better mitigate surface model artifacts. For all rivers in the avulsion database, channel paths were drawn manually using NASA/USGS Landsat imagery taken closest in time immediately preceding an avulsion event. For narrower, < 30 m wide channels in upland regions, channel paths were drawn manually from high-resolution satellite/aerial imagery tiles supplied by Microsoft Bing using the QuickMapServices plugin in QGIS desktop. Floodplain masks were drawn manually to ensure that floodplain swaths did not include higher elevation areas within 10 channel-widths either side of mapped channel. We also manually ensured that the effects of obvious topography above floodplain, structures, and other human-made objects were not included in our floodplain masks. We did not sample elevations along the channel profiles and our floodplain masks captured the broad elevation changes along the floodplain upstream and downstream of the avulsion sites. When adjacent hillslope elevation was to be measured for topographic swath profiles, unmasked elevation models were used in order to capture changes in channel confinement (Fig. S2).

We centered the elevation profiles on the avulsion sites, and measured elevations within 10 channel-widths either side of the channel. The longitudinal extent of the profiles extended 40 channel-widths upstream and downstream of avulsion sites. We used a SavGol filter on the profiles to reduce the noise. We visually ensured that the data were not oversmoothed with too large of a convolution window, so each river had a manually chosen window size that best captured the trends in the raw elevation data. To assess major topographic changes in valley slope or confinement across the avulsion sites, we computed the topographic slope-break in the swath profiles by estimating the local slope upstream and downstream of the avulsion sites; where 5 slope measurements were taken (a minimum 1 km bin length) with two bins dividing each study reach upstream and downstream of the avulsion node (~20 x channel width for each bin). We recorded the median and interquartile range of the slope for each bin. When avulsion sites were less than 20 channel widths from the shore, local slopes estimates were collated into a single downstream bin of length L_A.

Our results demonstrated all avulsions on fans and fan-deltas were associated with at least a threefold topographic slope-break in the swath profiles. The topographic slope-break in these profiles is indicative of an abrupt change in valley confinement, consistent with classical views of drivers of avulsions on fans. The abrupt change in valley-confinement on fans was further exemplified by the deviation of the channel-floodplain and valley profiles across the avulsion sites (Fig. S2; Fig. 1 in main text). Only one fan in our compilation (Fig. S3) did not show an apparent slope-break in the topographic swath profile because of backfilling of the fan. However, the avulsion site on this fan in Ethiopia was tied to abrupt valley-confinement change as evidenced by radially-emanating topographic profiles outside of the main fan (Fig. S3).

Text S3: Estimation of river morphometry to test the controls of avulsion locations on deltas

We compared the measured avulsion length on deltas with the estimated backwater lengthscale to test the emerging backwater theory for avulsions (*9*, *11*, *12*, *22*, *25*) (Fig. S4). We computed

the backwater lengthscale by estimating the riverbed slope, *S,* and the bankfull flow depth, h_{bf}, upstream of the avulsion site (*45*).

a. Riverbed slope

Previous researchers had estimated *S* in the field for some of the study reaches in our compilation, and we directly used these estimates for the computation of the backwater lengthscale (Table S1; compiled in (*11–13*, *22*, *33*, *34*)). When field measurements of *S* were not available, we used a global geospatial dataset of river slope, computed from the 15arc-sec resolution HydroSHEDS DEM and stream network (*46*). We validated this model using 42 measured riverbed slopes that spanned 5 continents, which were previously reported in the literature (*22*, *33*, *46*). We found the measured and estimated riverbed slopes were in close agreement, with the ratio of the measured and estimated values having a mean and median of 1.07 and 0.93, respectively (Fig. S5). The 1st and 3rd quartiles of the ratio of measured and estimated riverbed slopes were 0.66 and 1.33, respectively, with a minimum and maximum value of 0.12 and 2.78, respectively (Fig. S5).

When the 15arc-sec resolution was too coarse for computation of *S* (i.e., when multiple rivers are present within the single pixel at that resolution), we approximated *S* as the channel-floodplain slope in the masked composite SRTM and AW3D30 data (Text S2), following previous work (*31*). Rivers within the backwater zone typically have low sinuosity, and hence the floodplain slope is a reasonable approximation of the riverbed slope. All the riverbed slopes used in this study are tabulated in Table S1.

b. Bankfull flow depth

We used the field measured values of bankfull flow depth upstream of the avulsion site when reported by previous authors (compiled in (*11–13*, *22*, *33*, *34*)). In the absence of field estimates, we used an empirical approach modified from the river morphology module in the CaMa-Flood model (*47*), following (*32*):

$$h_{bf} = Max[0.5\bar{Q}^{0.3}, 1.0] \qquad \text{(S1)}$$

where $\bar{Q}$ is the long-term average water discharge, estimated from a global monthly dataset of water discharge over the last four decades (*32*). To test the validity of equation S1, we compiled

h_{bf} or the median bed-material grain size for a subset of rivers such that h_{bf} can be estimated from an empirical bankfull Shields stress criterion (*48*). Across the 16 rivers in this subset, equation S1 provided an accurate prediction of h_{bf}. Importantly, we found that equation S1 provides a reasonable approximation of h_{bf} for study reaches that cover the entire spectrum of flow depths from ~1 m to 20 m. The mean and the median of the ratio of measured and estimated bankfull flow depths were 1.06 and 0.83, respectively. The 1st and 3rd quartiles of the ratio of measured and estimated bankfull flow depths were 0.63 and 1.14, and the minimum and maximum values of this ratio were 0.52 and 3.35, respectively (Fig. S5).

c. Quantifying uncertainty in modeled slope and bankfull flow depth

We quantified the uncertainties in modeled S and h_{bf} using the ratio of the measured and estimated quantities shown in Figure S5. For each quantity, denoted here as X, we quantified the expected value and the uncertainty as follows:

$$\hat{X} = median\left(X_{meas}/X_{pred}\right) \times X_{pred} \quad \text{(S2)}$$

$$\delta\hat{X} = 0.5 \times IQR\left(X_{meas}/X_{pred}\right) \times X_{pred} \quad \text{(S3)}$$

where the subscripts *meas* and *pred* denote the measured and predicted values of the quantity of interest. This uncertainty in modeled riverbed slope and bankfull flow depth was carried over into the estimation of the backwater lengthscale and the dimensionless flood duration and dimensionless avulsion length.

d. Estimation of backwater lengthscale

We approximated the length over which nonuniform flows prevail due to the standing body of water in the receiving basin using the backwater lengthscale given by (*45*):

$$\overline{L_b} = \frac{h_{bf}}{S} \quad \text{(S4)}$$

Where available, we used field estimates of h_{bf} and S to compute the backwater lengthscale. In the absence of field estimates, we computed the backwater lengthscale by following the methodologies outlined in previous subsections to evaluate the bankfull flow depth and the riverbed slope. The uncertainty in the estimated backwater lengthscale was computed as:

$$\delta\overline{L_b} = \overline{L_b}\sqrt{\left(\frac{\delta h_{bf}}{h_{bf}}\right)^2 + \left(\frac{\delta S}{S}\right)^2} \quad \text{(S5)}$$

We used equations (S2) and (S3) when modeled flow depth and riverbed slope were used for the computation of the backwater lengthscale. When we approximated the slope using the SRTM/AW3D30 data, we evaluated the uncertainty of estimated *S* as the spread of local slopes measured within a single window of size 20x channel width, following previous work (*31*). We reported the estimates from equations (S4) and (S5) for each delta avulsion as the marker and the error bar in Figure 3A of the main text, respectively.

Finally, for all study reaches, we estimated the long-term water discharge, and the long-term suspended sediment discharge from the WBMSed model (*32*). This model was previously used to quantify the morphological response of global river deltas to deforestation, relative sea-level changes, and classify the delta morphology (*36*, *49*).

We also note that our global database of avulsions on river deltas are inconsistent with the emerging geometric hypothesis for avulsions on deltas (*23*). Using numerical models, it has been recently argued that backwater-scaled avulsions on deltas can arise from purely geometric constraints, without the need for flood discharge variability (*11*, *23*). In this scenario, avulsions are set up by the geometry of the prograding delta lobe. Geometrical constraints dictate that the active delta lobe must prograde by a distance that scales with the backwater lengthscale for the riverbed to aggrade by an amount that scales with the bankfull flow depth at the avulsion site, which leads to backwater-scaled avulsions, only if the floodplain elevation is held at sea level (*11*, *23*). However, the lack of a slope-break in the floodplain elevation profiles coincident with the avulsion location (Fig. 2), the scaling of the avulsion length with the backwater lengthscale only for rivers with $T_e^* \lesssim 1$ and not for rivers with $T_e^* > 1$ are inconsistent with the geometric hypothesis for avulsions on deltas. These observations instead support the hypothesis that backwater hydrodynamics and flood variability are a key control on setting up avulsions on river deltas (*11*, *12*) (Fig. S4).

Text S4: Estimation of dimensionless flood-variability parameters

To evaluate the dependence of the dimensionless avulsion length on flood variability, we computed the dimensionless flood duration, given by (*11*, *31*):

$$T_e^* = \frac{t_{scour}}{t_{adj}} \quad \text{(S6)}$$

where t_{scour} is the typical duration of the bankfull-overtopping flood and t_{adj} is the bed-adjustment timescale, which is computed as (*11*, *29*, *33*):

$$t_{adj} = \frac{h_{bf}\overline{L_b}}{(1-\lambda_p)q_s} = \frac{h_{bf}\overline{L_b}W_{bf}}{(1-\lambda_p)Q_s} \quad \text{(S7)}$$

where W_{bf} is the bankfull channel width, $\lambda_p = 0.4$ is the bed porosity, and Q_s and q_s are the volumetric sediment flux and the unit volumetric sediment flux during bankfull-overtopping floods, respectively. In equations (S6) and (S7), we evaluated h_{bf} and $\overline{L_b}$ using methods outlined in Text S3, and we evaluated t_{scour} following previous work (*31*). We first approximated the bankfull discharge as the peak-annual water discharge with a recurrence interval of 2 years using the simulated monthly discharge data from 1980 to 2020 C.E. globally (*32*). We then equated t_{scour} to the continuous duration of time for which the monthly water discharge exceeded the bankfull water discharge (Fig. S6). Finally, we computed the mean and standard deviation of t_{scour} for every coastal and lacustrine river in our compilation. The typical flood duration was well constrained across the global rivers with a mean and standard deviation of 1.78 and 0.69 months, respectively, and a minimum and maximum of 1.07 and 6.13 months, respectively. We evaluated Q_s during bankfull-overtopping floods using the paired data of simulated monthly water and suspended discharge for each study reach (*32*). For each duration of t_{scour}, we computed Q_s as the total volume of simulated suspended sediment discharge during bankfull-overtopping flood normalized by the duration t_{scour}. We then computed the mean and standard deviation of Q_s during each flood on record in the simulated time series of 40 years. To evaluate q_s, we normalized Q_s by the bankfull channel width, which was approximated using an empirical approach modified from the river morphology module in the CaMa-Flood model (*47*), following (*32*):

$$W_{bf} = Max[15\bar{Q}^{0.5}, 10] \quad \text{(S8)}$$

We note that the modeled total suspended discharge is an upper bound for the bed-material load during floods. The WBMSED 2.0 model provides a reasonable approximation of sediment discharge when compared against field observations (a coefficient of determination of 0.66 (*32*)); however, accurate sediment discharge measurements are challenging and the model data should be considered as estimates. While the bed-material load of gravel and sand-bedded rivers is dominated by suspended sediment load during floods (*50*, *51*), the fraction of wash load in the suspended sediment discharge can be variable. For example, numerical models indicate that the

average fraction of wash load in the suspended sediment discharge for the rivers in contiguous United States is approximately 62% (*52*), and recent work also indicates that wash load in coastal environments may interact with the bed because of mud flocculation (*53*). The partitioning of total suspended sediment discharge into wash load and suspended bed-material load and the model uncertainties may impact our estimates of the dimensionless flood duration; however, these variations are likely to be small compared to the 8 orders-of-magnitude variation observed in the dimensionless flood duration for our global compilation.

We computed the representative value of T_e^* for each river using the mean quantities in the right-hand side of equation (S6) and evaluated the uncertainty in T_e^* using:

$$\frac{\delta T_e^*}{T_e^*} = \sqrt{\left(\frac{\delta t_{scour}}{t_{scour}}\right)^2 + \left(\frac{\delta q_s}{q_s}\right)^2 + \left(\frac{\delta \overline{L_b}}{\overline{L_b}}\right)^2} \quad \text{(S9)}$$

where $\delta(.)$ denotes the standard deviation of the quantity. In Figure 3B of the main text, we plotted the mean and standard deviation of the dimensionless flood duration. In our database, 19 of the 50 backwater-scaled avulsions had a mean T_e^* value less than 0.1, and 31 of the 50 backwater-scaled avulsions had a mean T_e^* value between 0.1 and 2 (Fig. 3B). All but 2 of the high-sediment-load modulated avulsions had a mean T_e^* value greater than 1. The sparsity of the avulsions on deltas with a very small T_e^* value is likely in part due to the fact that large, lowland rivers avulse infrequently, and the historical satellite record is limited in time. Moreover, the number of large, lowland rivers on our planet are low owing to the nature of the drainage network organization.

We found that $T_e^* \approx 1$ demarcates the backwater-scaled avulsions from the high-sediment-load modulated avulsions, consistent with physics-based numerical models for deltaic avulsions that include the effects of backwater hydrodynamics (*11*, *30*). A loess regression to the data of dimensionless avulsion length and dimensionless flood duration revealed that L_A^* deviated from a value of 1 at $T_e^* \approx 0.75$. The 95% confidence bounds on the T_e^* value where L_A^* deviated from 1 is 0.2 and 2. To assess if T_e^* separates the avulsions into two separate regimes, we binned the L_A^* values into 3 categories: rivers with $T_e^* < 0.1$, rivers with $T_e^* \in [0.1, 2]$, and rivers with $T_e^* > 2$. We found that the L_A^* values for the first two categories were similar (Fig. S7; two-sample t-test yielded a *P*-value of 0.53), consistent with the backwater-avulsion theory and numerical models. In contrast, the L_A^* values were greater than 1 for rivers with $T_e^* \gg 1$ indicating that the dimensionless flood duration is a fundamental control on the avulsion length in river deltas. Furthermore, the L_A^* value in category 3 ($T_e^* > 2$) was statistically different from

the L_A^* value in both the category 2 ($T_e^* \in [0.1, 2]$; two-sample t-test yielded a *P*-value of 1.2×10^{-7}) and category 1 ($T_e^* < 0.1$; two-sample t-test yielded a *P*-value of 3.1×10^{-4}).

Our results indicate that rivers with $T_e^* \in [0.1, 2]$ are likely to be susceptible to transition into the high-sediment-load modulated avulsion regime with future changes in climate and land use. This is because an increase in either the flood duration, magnitude and/or the sediment supply can transition the T_e^* value beyond 1, pushing the avulsions from the backwater-scaled to the high-sediment-load modulated regime. Rivers with $T_e^* \in [0.1, 2]$ corresponded to small inland river deltas (e.g., Sulengguole river delta) and low-gradient tropical deltas with high sediment supply, e.g., deltas in Indonesia (Fig. S8). These deltas have a bed-adjustment timescale on the order of months (Fig. S8). In contrast, large, low-gradient deltas had a dimensionless flood duration less than 0.1 (Fig. S8), indicating that these deltas require an order-of-magnitude change in flood magnitude and/or duration to transition into the high-sediment-load modulated avulsion regime. The rivers with high-sediment-load modulated avulsions corresponded to steep, sediment-laden rivers in desert environments and in tropical islands, which had a dimensionless flood duration much greater than 1 (Figs. S9, S10). Moreover, our data demonstrate high variability in L_A^* for rivers with T_e^* values close to 1, consistent with numerical models (*11*, *30*). The flood-scour length determines the minimum upstream extent at which avulsions will likely occur in deltaic environments and $\overline{L_b}\sqrt{T_e^*}$ provides a theoretical expectation of this quantity (*31*). However, the temporal sequence of flood duration and magnitude can be an important factor for rivers with T_e^* close to 1 because closely spaced floods can cause the amalgamation of scours leading to $L_A^* > 1$.

We also used the global simulated monthly water discharge time series to quantify the probability of bankfull exceedance, F_{bf}, for each river with deltaic avulsions, which was defined as:

$$F_{bf} = \frac{n \times t_{scour}}{T} \quad \text{(S10)}$$

where n is the number of bankfull-overtopping floods in the 40-year record (Table S1), t_{scour} is the average flood duration for each study reach, and T is the total duration of the record, which is 40 years. Finally, we quantified the degree to which a river was ephemeral by accounting for the number of months on record for which the flow was less than 0.01 m^3/s.

Text S5: Quantifying the mobility of backwater-scaled avulsion sites

We followed previous work to quantify the coevolution of avulsion sites and river mouth for the deltas with multiple recorded avulsions (*9*, *13*, *35*). The evolution of the avulsion sites and the river mouth have previously been quantified for the Huanghe (*9*, *13*) and the Sulengguole River deltas (*35*). For the Cipunagara and Cisanggarung river deltas, we chose a fixed reference point upstream of the historical avulsion sites (Figs. 4A, B, S11). We then characterized the streamwise distance of the river mouth to this fixed reference point each year from the satellite imagery. Similarly, we also quantified the streamwise distance between the historical avulsion site and the fixed reference point. We then normalized both these quantities by the backwater lengthscale of each river. Finally, we fit a linear model between the normalized river-mouth location and time, and the normalized avulsion location and time in MATLAB. In Figure 4C of the main text, we reported the mean and the 95% confidence interval of the best-fitting regression line for each delta. The consistency between the regression slopes of normalized river-mouth evolution and normalized avulsion-site migration indicates that the avulsion sites migrated in tandem with river-mouth evolution such that the avulsion length was consistent with time for each delta.

Text S6: Impact of earthquakes on river avulsions

We assessed the degree to which earthquakes impacted river avulsions in our global database. Earthquakes can cause liquefaction at significant distances away from the epicenter (*54*), which could lead to levee failure that triggers an avulsion. Earthquakes have also been shown to transiently increase streamflow in the far field, and the distance away from the earthquake epicenter over which this effect is observed is similar to that of liquefaction (*55*, *56*). We used a global observational database of earthquake magnitude (M_w) and the distance away from the earthquake epicenter (R_{max}) where liquefaction was observed (*54*) to constrain the potential avulsions that are likely impacted by avulsions (Fig. S12). We binned M_w into 5 bins: M_w 5-6, M_w 6-7, M_w 7-8, M_w 8-9 and M_w 9-10 (Fig. S12). Within each bin, we estimated the 95th percentile of the observed distances over which liquefaction has been reported (Fig. S12). We then leveraged the global database of earthquakes (available at: https://earthquake.usgs.gov/earthquakes/search/) to ascertain the number of earthquakes within a radius of R_{max} from each avulsion site that occurred in the year of avulsion or the previous calendar year. Our results revealed that only 8 avulsions in our database were likely impacted by

earthquakes. Of these 8 avulsions, 4 were deltaic avulsions and 4 were avulsions observed on fan-deltas. This analysis demonstrated that only a small fraction of the observations of avulsions were likely impacted by earthquakes.

5

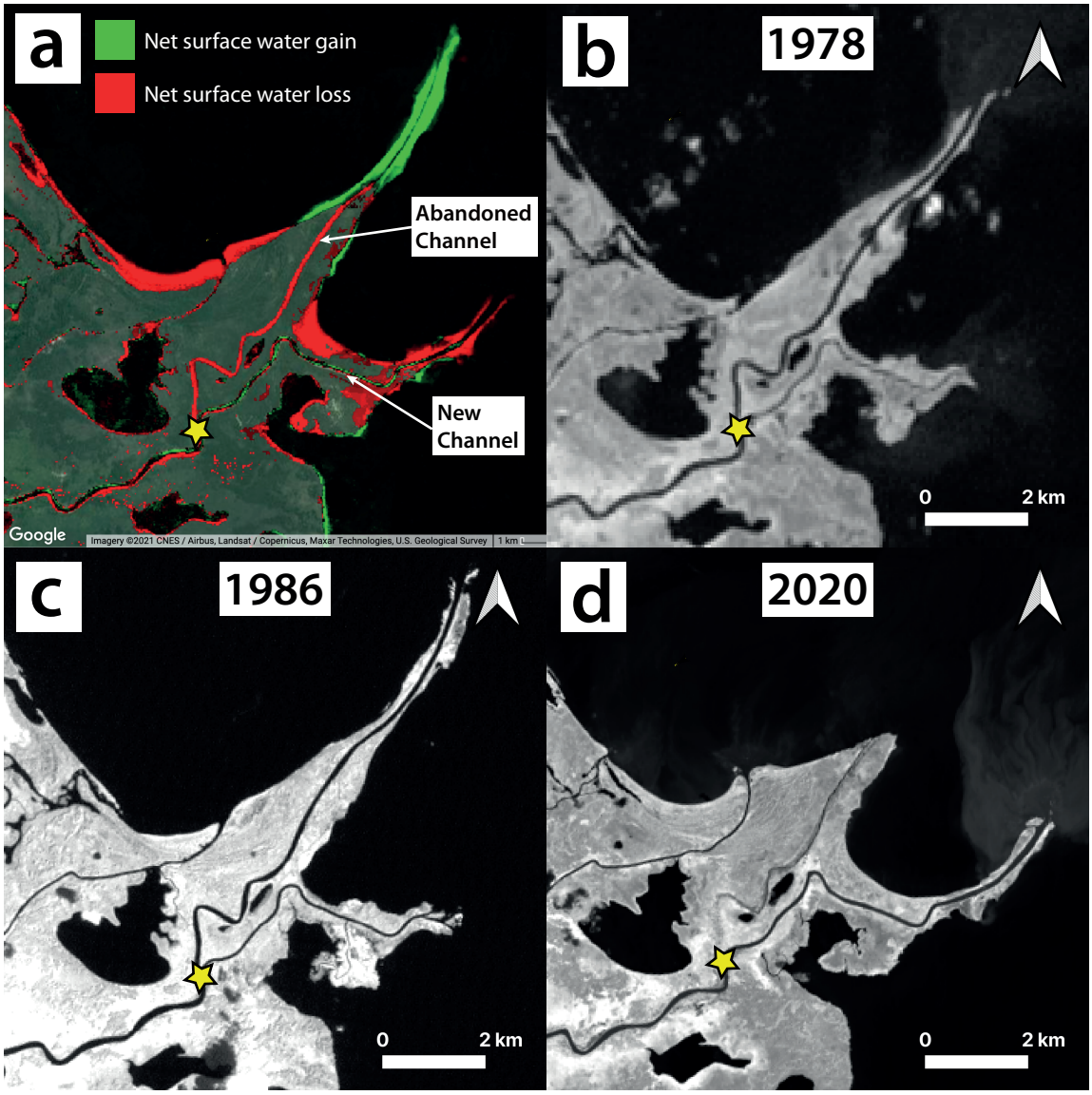

Fig. S1. Example identification of the avulsion site on the Catatumbo River delta, Venezuela, using (a) surface water change layers in Google Earth Engine from the Pekel et al. (*18*) global surface water dataset and (b-d) Landsat 2, 5 and 8 NIR imagery in time series. a) Green regions show areas of net surface water gain between 1984-2020 C.E. and red areas a net loss of surface water over the same period. Delta-lobe abandonment is clear from the shoreline retreat and land loss at former river mouth, with a simultaneous loss of surface water within its abandoned channel. The now active, southern delta lobe shows a loss in net surface water owing to delta lobe progradation. Time series of Landsat NIR imagery shows the changing delta morphology between 1978 and 2020 C. E., with the avulsion site marked by a yellow star.

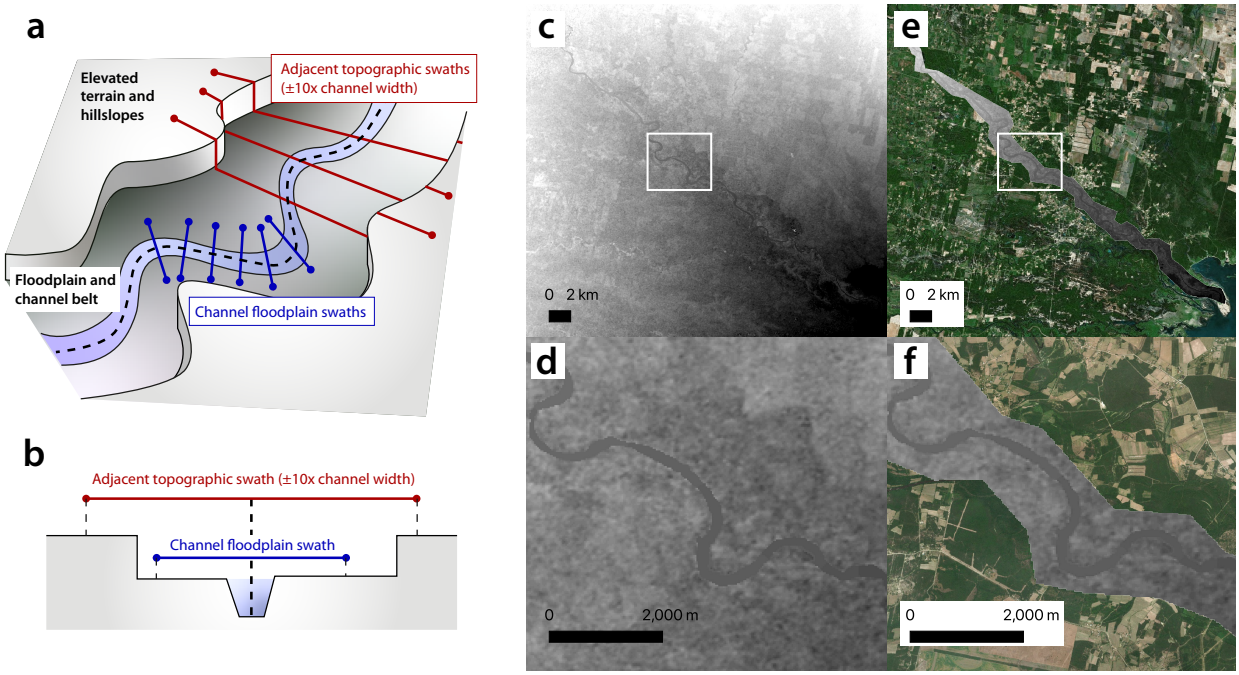

Fig. S2. a & b) Schematics of the elevation profiles measuring change in elevation nearest to the channel (blue lines), with larger (10x channel width) swaths capturing increases in elevation, and subsequently channel belt confinement (red lines). Example application of this methodology to the Salí River, Argentina, where panel c shows the unmasked SRTM DEM. d) Closer view of unmasked channel belt. e) Extent of surface model after application of floodplain mask. f) Closer view of masked floodplain elevation model.

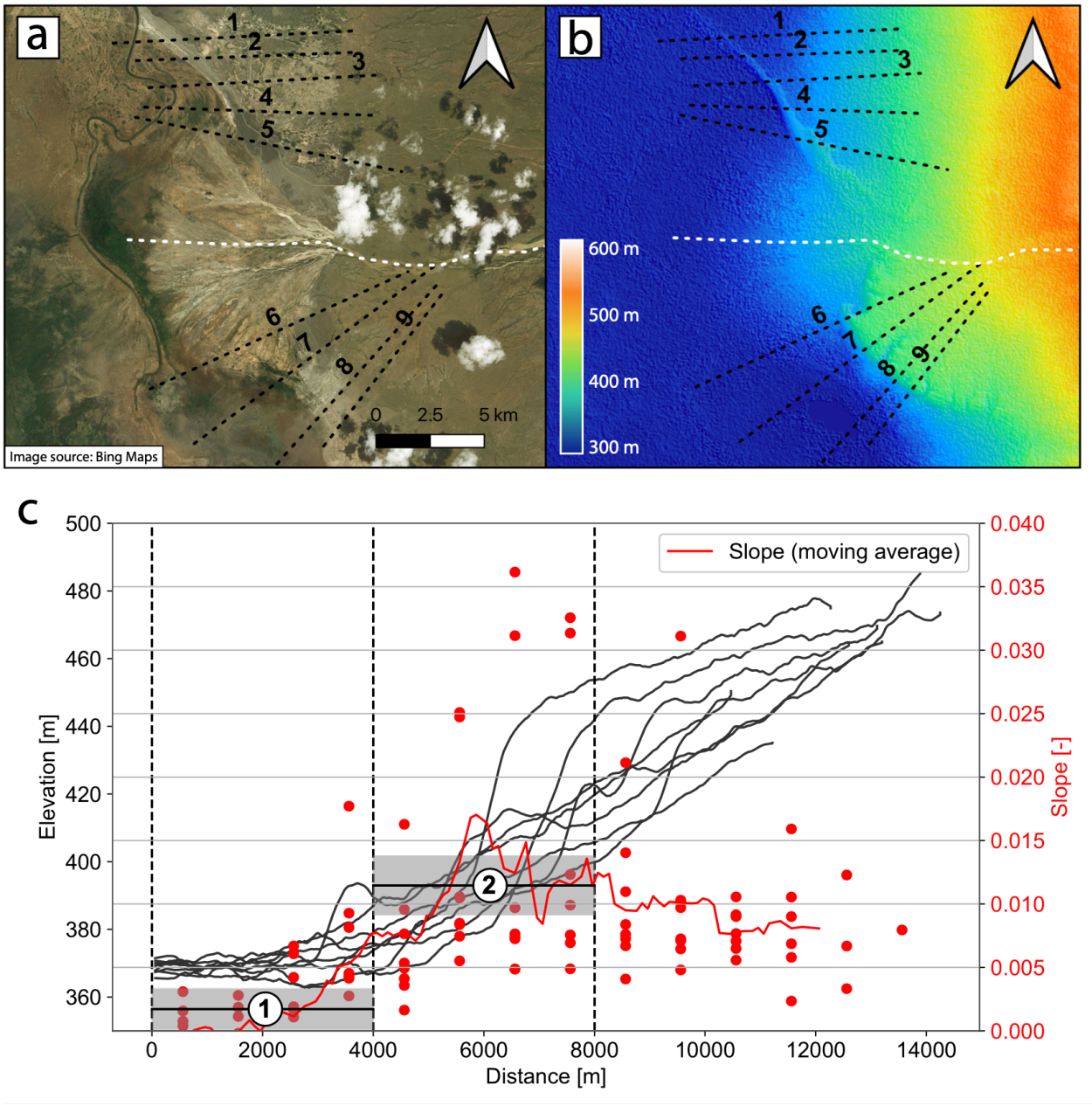

Fig. S3. a. Aerial imagery of backfilled fan in Ethiopia (36.17867E ,4.70719N) where elevation profiles were taken along the main fan (white dashed line) and 9 adjacent transects (black dashed lines). The backfilling of the fan concealed the topographic confinement change at the avulsion site when topographic swaths was taken along the channel profile (white dashed line). However, the confinement change is apparent when topographic swath profiles were considered outside the fan and within the SRTM data. b. SRTM elevation model of fan and adjacent slopes. c. West to east elevation profiles were measured for all slope transects, encompassing the main fan and areas < 10 km north and south of the fan apex. Local slope measurements (red dots) binned 4 km

upstream and downstream of the approximate avulsion location show a 6.7x slope change of between bins 1 (0.0017) and 2 (0.0115). All other fan avulsions showed a topographic slope-break in elevation profiles taken along the longitudinal extent of the channel.

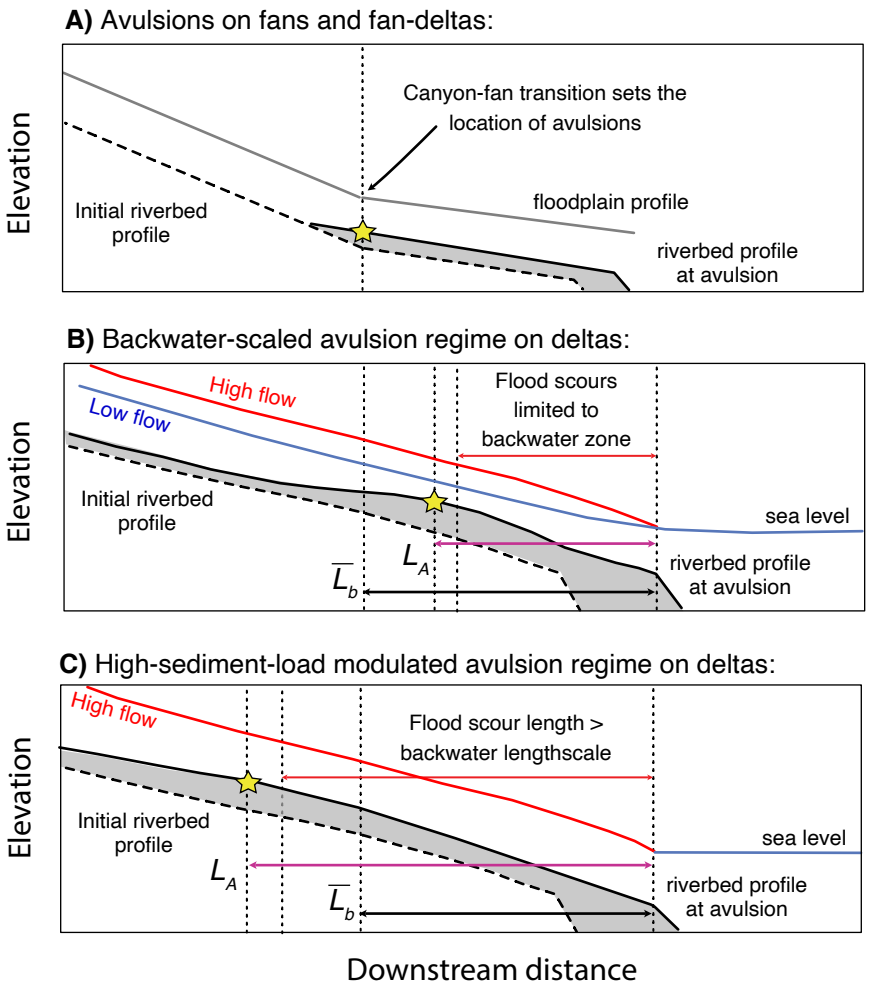

Fig S4. The mechanisms that setup avulsions on (A) fans, (B) river deltas with $T_e^* \lesssim 1$, and (C) river deltas with $T_e^* > 1$. Avulsion setup refers to the process of preferential riverbed aggradation that perches a channel above its surrounding floodplain that renders the channel unstable (*14*). (A) On fans, the location where the channels are critically superelevated above the surrounding floodplain coincides with an abrupt topographic change (e.g., a change in riverbed slope or valley confinement), leading to the propensity for avulsions at the canyon-fan transition (*1*, *20*, *21*, *57*). In contrast, avulsion sites on deltas are typically not associated with a canyon-fan transition. Instead, riverbed aggradation is driven by the progradation of the delta lobe, and numerical models and physical experiments demonstrated that backwater hydrodynamics and flood variability focus aggradation within the upstream portion of the backwater zone leading to avulsions there (*11*, *12*, *22*, *30*). During low flows (blue line), rivers decelerate in approach to their basin leading to sedimentation within the backwater zone (*26*, *27*). However, floods (red line) cause spatial acceleration of flow towards the river mouth resulting in erosional scours that

diminish sedimentation within the flood-scour zone. The flood-driven scours are typically limited to the backwater zone on large, low-gradient rivers (*27*), causing the scaling between the avulsion length and the backwater lengthscale (B). However, the flood-driven scours can extend beyond the backwater zone for rivers with short bed-adjustment timescale with respect to the flood duration (*31*, *33*) such that sedimentation is diminished within the flood-scour zone, leading to avulsions upstream of the flood-scour and backwater zones (C) (*11*, *12*, *22*). Theory and numerical models indicate that flood-scour lengthscale can exceed the backwater lengthscale when the bed-adjustment timescale is less than the typical flood duration, i.e., $T_e^* > 1$ (*11*, *31*). Therefore, T_e^* is expected to separate the backwater-scaled avulsion regime (B) from the high-sediment-load modulated regime (C). In all cases, the dashed and solid lines indicate the initial and final riverbed profile during an avulsion cycle, respectively, the shaded area denotes the amount of sedimentation that occurred during an avulsion cycle, and the yellow star indicates the avulsion site.

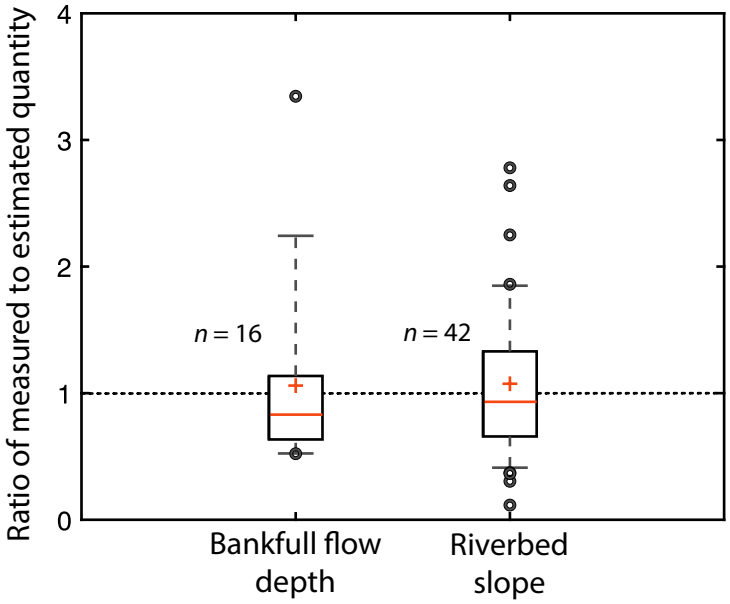

Fig. S5. Box plots of the ratio of the measured to estimated bankfull flow depth and riverbed slope. The measured values are reported bankfull flow depth (*11–13*, *22*, *33*, *34*) and riverbed slope (*22*, *33*, *46*) from previous studies and the estimated values are using equation (S1) and the Global Geospatial Riverbed slope database of Cohen et al. (*46*).

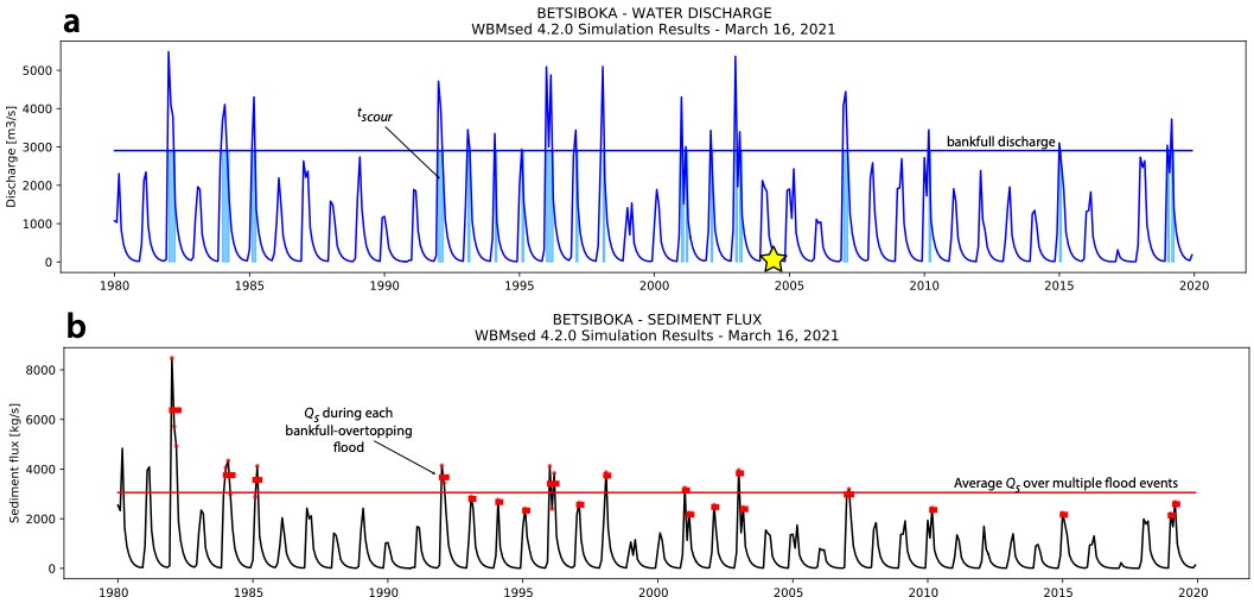

Fig. S6. Example computation of typical flood duration and the sediment flux during the bankfull-overtopping floods for the Betsiboka river in Madagascar. a) Time series of monthly simulated water discharge from 1980 to 2020 C.E. where the bankfull water discharge is approximated as the 2-year recurrence interval, peak-annual flood (blue horizontal line). The typical flood duration is the average of the continuous durations for which bankfull-overtopping floods occurred in the last 40 years (translucent blue bars). b) Paired time series of monthly suspended sediment flux data with red squares indicating the average sediment flux during the bankfull-overtopping floods, which was computed as the area under the sediment flux time series during t_{scour}, normalized by t_{scour}.

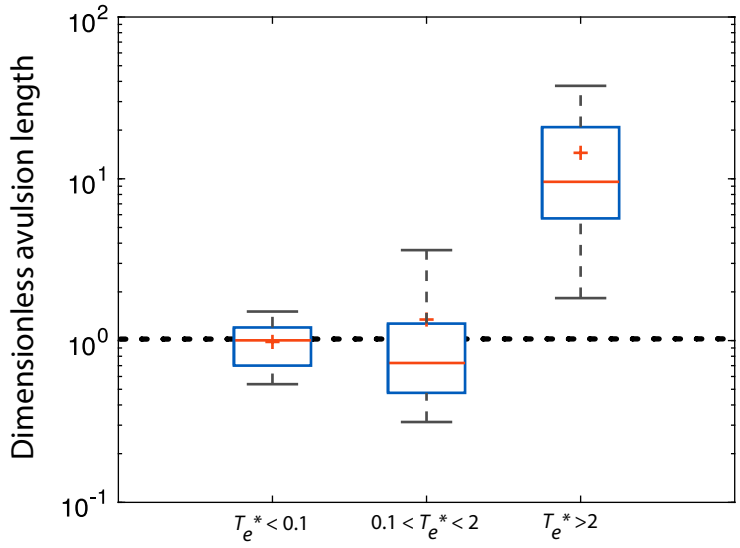

Fig. S7. Comparison of the dimensionless avulsion length for rivers with $T_e^* < 0.1$, $T_e^* \in [0.1, 2]$, and $T_e^* > 2$. The dashed line indicates the dimensionless avulsion length of 1, which approximates a backwater-scaled avulsion node. The red line and plus sign indicate the median and the mean, respectively, with the edges of the box denoting the 1st and 3rd quartiles. The edges of the whiskers denote the 9th and 91st percentile of the data within each category.

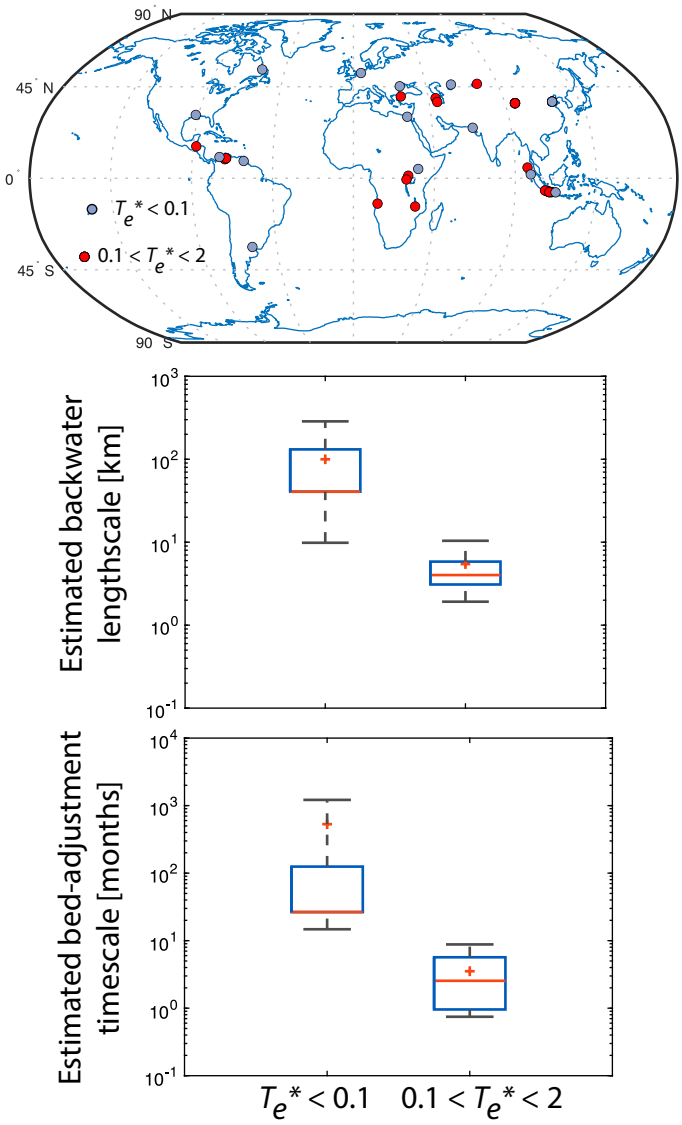

Fig. S8. (top panel) Global distribution of avulsion sites on river deltas with $T_e^* < 0.1$ and $T_e^* \in [0.1, 2]$. Comparison of the estimated backwater lengthscale (middle panel) and the estimated bed-adjustment timescale (bottom panel) for rivers with with $T_e^* < 0.1$ and $T_e^* \in [0.1, 2]$. The red line and plus sign indicate the median and the mean, respectively, with the edges of the box denoting the 1st and 3rd quartiles. The edges of the whiskers denote the 9th and 91st percentile of the data within each category.

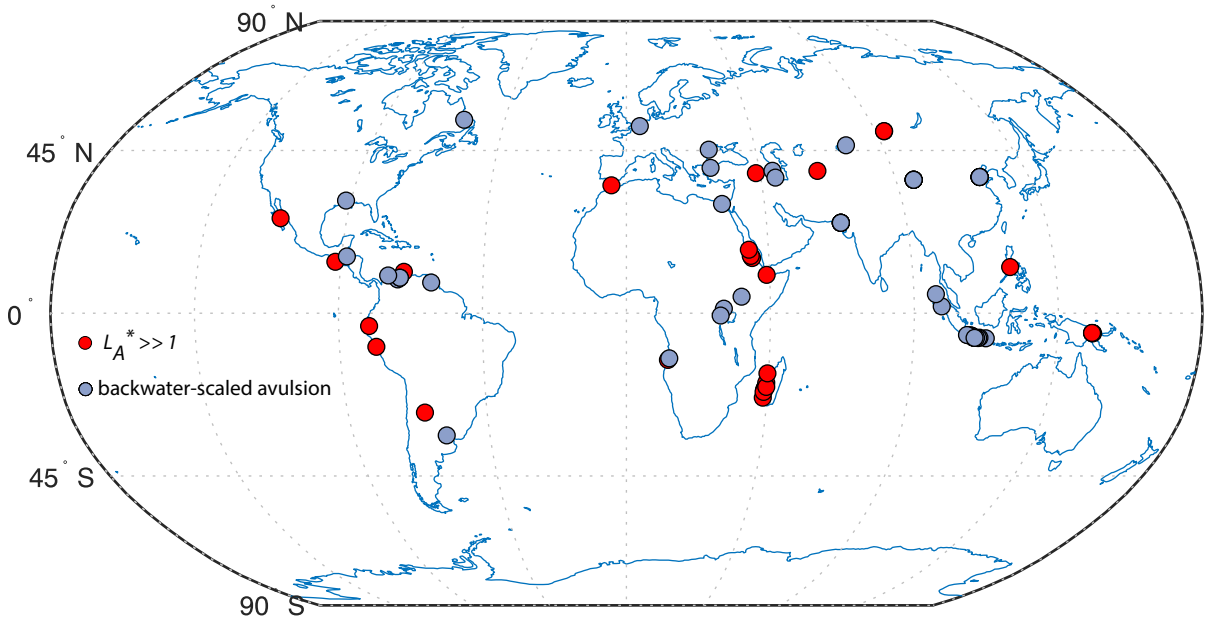

Fig. S9. Global distribution of avulsion sites on river deltas. The blue markers denote backwater-scaled avulsion sites with $L_A \approx \overline{L_b}$, and the red markers denote river avulsions with $L_A \gg \overline{L_b}$.

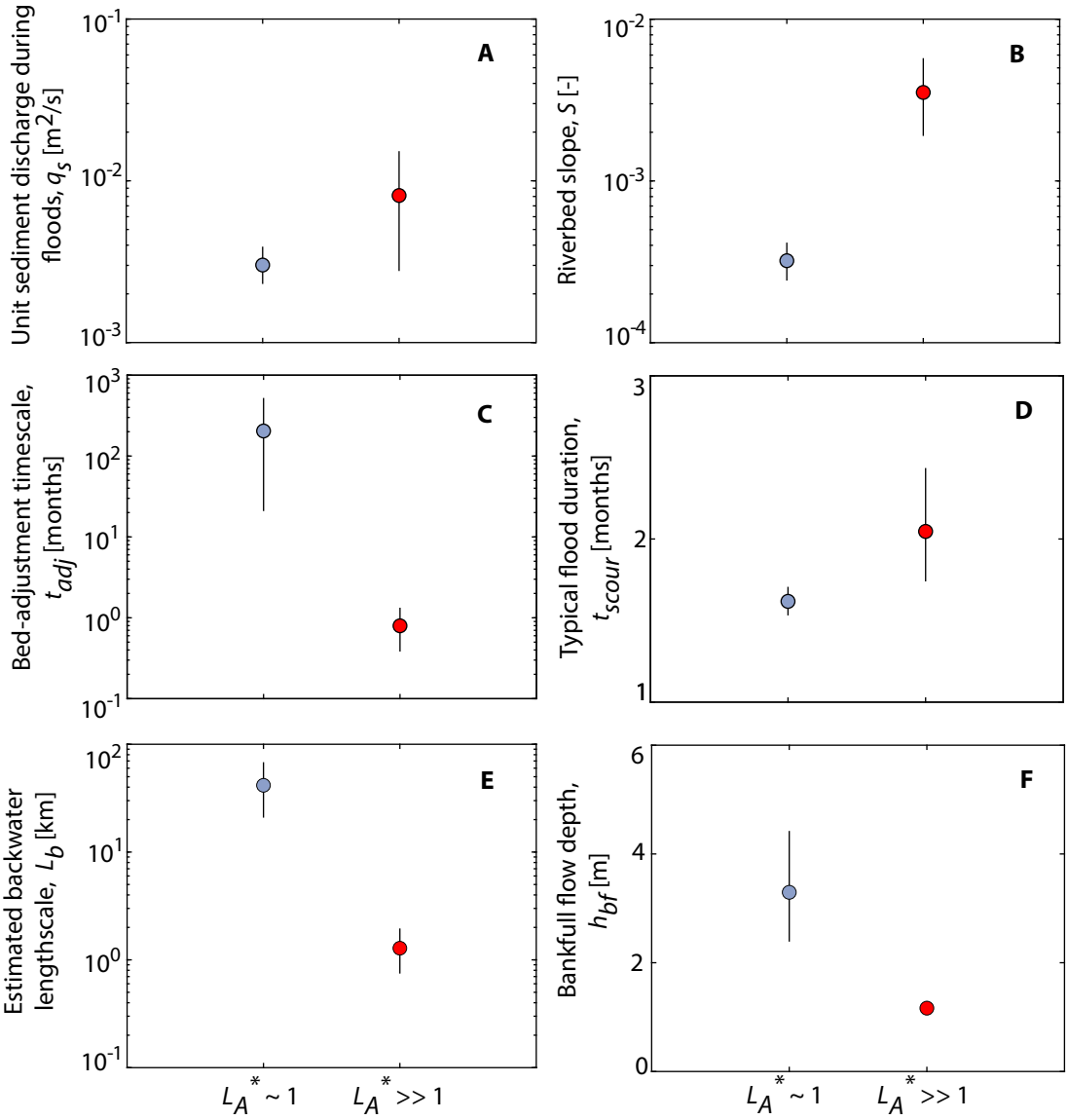

Fig. S10. Comparison of the (A) unit sediment discharge during floods, (B) riverbed slope, (C) bed-adjustment timescale, (D) typical flood duration, (E) estimated backwater lengthscale, and (F) bankfull flow depth between river deltas with backwater-scaled avulsions ($L_A \approx \overline{L_b}$; blue markers; n = 50) and high-sediment-load modulated avulsions ($L_A \gg \overline{L_b}$; red markers; n = 30). The markers denote the mean and the error bar denotes the 95% confidence interval on the mean, computed using the bootstrapping method.

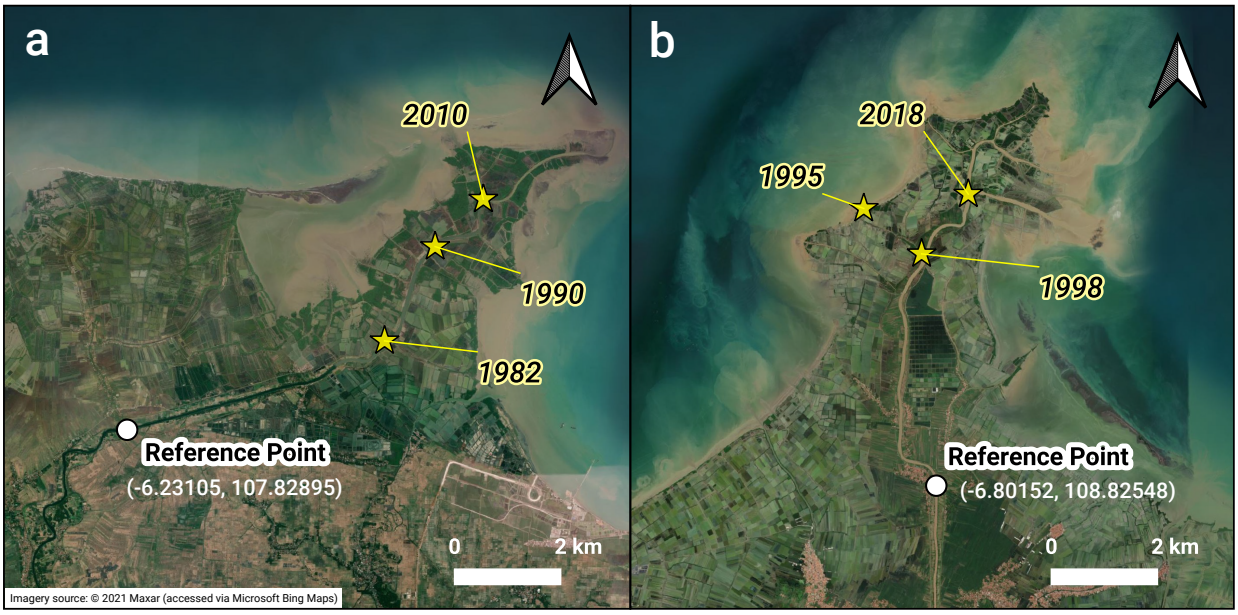

Fig S11. Satellite images of the Cipunagara and Cisanggarung rives in Indonesia. The white markers indicate the reference point (along with coordinates) for these rivers, which was used for quantifying the temporal evolution of the river mouth and the avulsion sites (Fig. 4C in main text). We measured the streamwise distance of the avulsion sites and the river-mouth location in each year, and normalized these distances by the backwater lengthscale (Figure 4C of the main text).

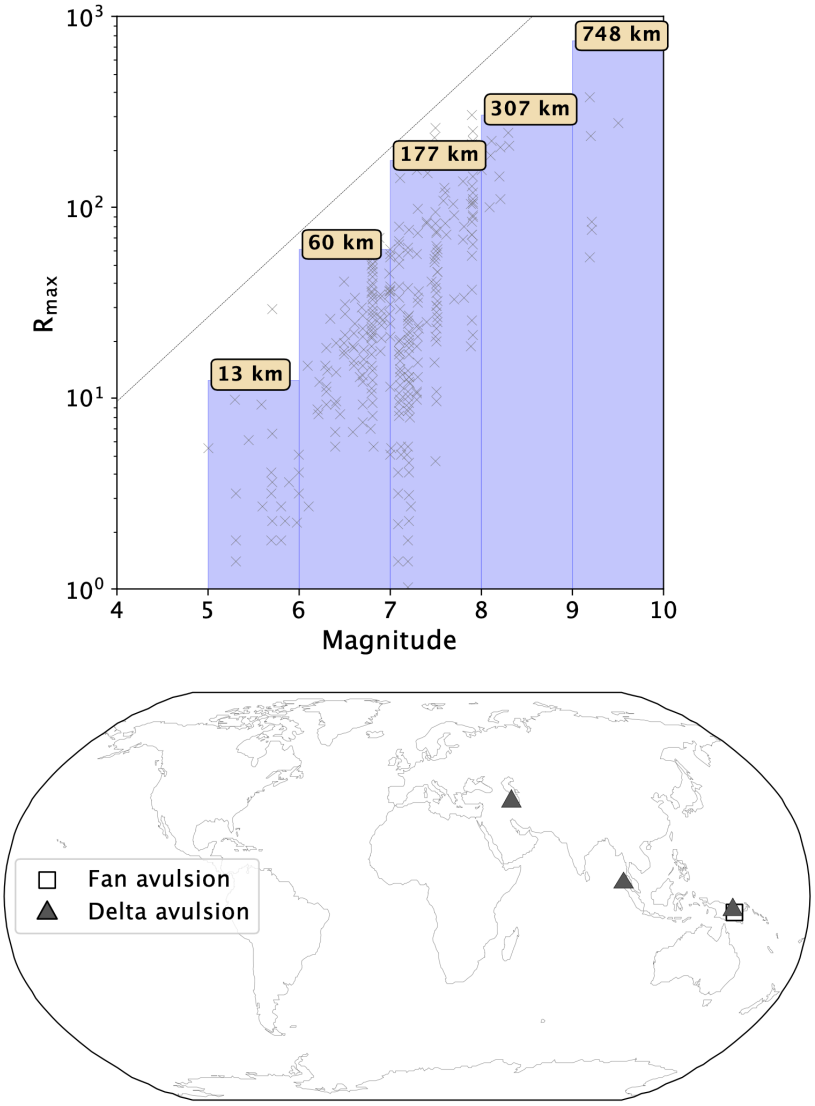

Fig. S12. (top panel) Empirical observations of the distance away from the earthquake epicenter where liquefaction was observed (cross markers) as a function of the magnitude of the earthquake (data reproduced from (*54*)). The blue bars show the binned earthquake magnitude data and the 95th percentile of the observations used for identifying avulsions that were likely influenced by earthquakes. (bottom panel) The avulsion sites in our global database that had an earthquake magnitude greater than 5 within a proximal distance determined by the top panel.

References and Notes

1. R. Slingerland, N. D. Smith, River avulsions and their deposits. *Annu. Rev. Earth Planet. Sci.* **32**, 257–285 (2004). doi:10.1146/annurev.earth.32.101802.120201

2. C. J. Vörösmarty, J. Syvitski, J. Day, A. de Sherbinin, L. Giosan, C. Paola, Battling to save the world's river deltas. *Bull. At. Sci.* **65**, 31–43 (2009). doi:10.2968/065002005

3. P. H. Gleick, Global Freshwater Resources: Soft-Path Solutions for the 21st Century. *Science* **302**, 1524–1528 doi:10.1126/science.1089967 (2003).

4. D. A. Edmonds, R. L. Caldwell, E. S. Brondizio, S. M. O. Siani, Coastal flooding will disproportionately impact people on river deltas. *Nat. Commun.* **11**, 4741 (2020). doi:10.1038/s41467-020-18531-4 Medline

5. T. R. Kidder, H. Liu, Bridging theoretical gaps in geoarchaeology: Archaeology, geoarchaeology, and history in the Yellow River valley, China. *Archaeol. Anthropol. Sci.* **9**, 1585–1602 (2017). doi:10.1007/s12520-014-0184-5

6. R. Sinha, The great avulsion of Kosi on 18 August 2008. *Curr. Sci.* **97**, 429–433 (2009).

7. G. S. Morozova, A review of Holocene avulsions of the Tigris and Euphrates rivers and possible effects on the evolution of civilizations in lower Mesopotamia. *Geoarchaeology* **20**, 401–423 (2005). doi:10.1002/gea.20057

8. D. J. Jerolmack, Conceptual framework for assessing the response of delta channel networks to Holocene sea level rise. *Quat. Sci. Rev.* **28**, 1786–1800 (2009). doi:10.1016/j.quascirev.2009.02.015

9. V. Ganti, Z. Chu, M. P. Lamb, J. A. Nittrouer, G. Parker, Testing morphodynamic controls on the location and frequency of river avulsions on fans versus deltas: Huanghe (Yellow River), China. *Geophys. Res. Lett.* **41**, 7882–7890 (2014). doi:10.1002/2014GL061918

10. A. Aslan, W. J. Autin, M. D. Blum, Causes of river avulsion: Insights from the Late Holocene avulsion history of the Mississippi River, U.S.A. *J. Sediment. Res.* **75**, 650–664 (2005). doi:10.2110/jsr.2005.053

11. A. J. Chadwick, M. P. Lamb, A. J. Moodie, G. Parker, J. A. Nittrouer, Origin of a preferential avulsion node on lowland river deltas. *Geophys. Res. Lett.* **46**, 4267–4277 (2019). doi:10.2110/jsr.2005.053

12. V. Ganti, A. J. Chadwick, H. J. Hassenruck-Gudipati, B. M. Fuller, M. P. Lamb, Experimental river delta size set by multiple floods and backwater hydrodynamics. *Sci. Adv.* **2**, e1501768 (2016). doi:10.1126/sciadv.1501768 Medline

13. A. J. Moodie, J. A. Nittrouer, H. Ma, B. N. Carlson, A. J. Chadwick, M. P. Lamb, G. Parker, Modeling Deltaic Lobe-Building Cycles and Channel Avulsions for the Yellow River Delta, China. *J. Geophys. Res. Earth Surf.* **124**, 2438–2462 (2019). doi:10.1029/2019JF005220

14. D. Mohrig, P. L. Heller, C. Paola, W. J. Lyons, Interpreting avulsion process from ancient alluvial sequences: Guadalope-Matarranya system (northern Spain) and Wasatch Formation (western Colorado). *Geol. Soc. Am. Bull.* **112**, 1787–1803 (2000). doi:10.1130/0016-7606(2000)112<1787:IAPFAA>2.0.CO;2

15. O. A. Prasojo, T. B. Hoey, A. Owen, R. D. Williams, Slope break and avulsion locations scale consistently in global deltas. *Geophys. Res. Lett.*, ***49***, e2021GL093656 (2022).

16. D. A. Edmonds, A. J. Chadwick, M. P. Lamb, J. Lorenzo-Trueba, B. Murray, W. Nardin, G. Salter, J. B. Shaw, Morphodynamic Modeling of River-Dominated Deltas: A Review and Future Perspectives. ESSOAr 10507512.1 [Preprint] (2021); doi:10.1002/essoar.10507512.1.

17. J. M. Valenza, D. A. Edmonds, T. Hwang, S. Roy, Downstream changes in river avulsion style are related to channel morphology. *Nat. Commun.* **11**, 2116 (2020). doi:10.1038/s41467-020-15859-9 Medline

18. J.-F. Pekel, A. Cottam, N. Gorelick, A. S. Belward, High-resolution mapping of global surface water and its long-term changes. *Nature* **540**, 418–422 (2016). doi:10.1038/nature20584 Medline

19. Materials and methods are available as supplementary materials.

20. T. C. Blair, J. G. McPherson, Alluvial fans and their natural distinction from rivers based on morphology, hydraulic processes, sedimentary processes, and facies assemblages. *J. Sediment. Res.* **64**, 450–489 (1994).

21. L. S. Jones, S. A. Schumm, Causes of avulsions: An overview. *Spec. Publ. Int. Assoc. Sedimentol.* **28**, 171–178 (1999).

22. P. Chatanantavet, M. P. Lamb, J. A. Nittrouer, Backwater controls of avulsion location on deltas. *Geophys. Res. Lett.* **39**, n/a (2012). doi:10.1029/2011GL050197

23. K. M. Ratliff, E. W. H. Hutton, A. B. Murray, Modeling long-term delta dynamics reveals persistent geometric river avulsion locations. *Earth Planet. Sci. Lett.* **559**, 116786 (2021). doi:10.1016/j.epsl.2021.116786

24. V. Ganti, A. J. Chadwick, H. J. Hassenruck-Gudipati, M. P. Lamb, Avulsion cycles and their stratigraphic signature on an experimental backwater-controlled delta. *J. Geophys. Res. Earth Surf.* **121**, 1651–1675 (2016). doi:10.1002/2016JF003915

25. D. J. Jerolmack, J. B. Swenson, Scaling relationships and evolution of distributary networks on wave-influenced deltas. *Geophys. Res. Lett.* **34**, n/a (2007). doi:10.1029/2007GL031823

26. J. A. Nittrouer, J. Shaw, M. P. Lamb, D. Mohrig, Spatial and temporal trends for water-fl ow velocity and bed-material sediment transport in the lower Mississippi River. *Geol. Soc. Am. Bull.* **124**, 400–415 (2012). doi:10.1130/B30497.1

27. M. P. Lamb, J. A. Nittrouer, D. Mohrig, J. Shaw, Backwater and river plume controls on scour upstream of river mouths: Implications for fluvio-deltaic morphodynamics. *J. Geophys. Res.* **117**, 2011JF002079 (2012). doi:10.1029/2011JF002079

28. C. Paola, D. Mohrig, Palaeohydraulics revisited: Palaeoslope estimation in coarse-grained braided rivers. *Basin Res.* **8**, 243–254 (1996). doi:10.1046/j.1365-2117.1996.00253.x

29. P. Chatanantavet, M. P. Lamb, Sediment transport and topographic evolution of a coupled river and river plume system: An experimental and numerical study. *J. Geophys. Res. Earth Surf.* **119**, 1263–1282 (2014). doi:10.1002/2013JF002810

30. A. J. Chadwick, M. P. Lamb, Climate-Change Controls on River Delta Avulsion Location and Frequency. *J. Geophys. Res. Earth Surf.* **126**, e2020JF005950 (2021). doi:10.1029/2020JF005950

31. S. A. S. Brooke, V. Ganti, A. J. Chadwick, M. P. Lamb, Flood Variability Determines the Location of Lobe-Scale Avulsions on Deltas: Madagascar. *Geophys. Res. Lett.* **47**, (2020). doi:10.1029/2020GL088797

32. S. Cohen, A. J. Kettner, J. P. M. Syvitski, Global suspended sediment and water discharge dynamics between 1960 and 2010: Continental trends and intra-basin sensitivity. *Global Planet. Change* **115**, 44–58 (2014). doi:10.1016/j.gloplacha.2014.01.011

33. V. Ganti, M. P. Lamb, A. J. Chadwick, Autogenic Erosional Surfaces in Fluvio-deltaic Stratigraphy from Floods, Avulsions, and Backwater Hydrodynamics. *J. Sediment. Res.* **89**, 815–832 (2019). doi:10.2110/jsr.2019.40

34. A. J. Chadwick, M. P. Lamb, V. Ganti, Accelerated river avulsion frequency on lowland deltas due to sea-level rise. *Proc. Natl. Acad. Sci. U.S.A.* **117**, 17584–17590 (2020). doi:10.1073/pnas.1912351117 Medline

35. J. Li, V. Ganti, C. Li, H. Wei, Upstream migration of avulsion sites on lowland deltas with river-mouth retreat. *Earth Planet. Sci. Lett.* **577**, 117270 doi:10.1016/j.epsl.2021.117270 (2022).

36. J. H. Nienhuis, A. D. Ashton, D. A. Edmonds, A. J. F. Hoitink, A. J. Kettner, J. C. Rowland, T. E. Törnqvist, Global-scale human impact on delta morphology has led to net land area gain. *Nature* **577**, 514–518 (2020). doi:10.1038/s41586-019-1905-9 Medline

37. Y. Hirabayashi, R. Mahendran, S. Koirala, L. Konoshima, D. Yamazaki, S. Watanabe, H. Kim, S. Kanae, Global flood risk under climate change. *Nat. Clim. Chang.* **3**, 816–821 (2013). doi:10.1038/nclimate1911

38. D. A. Edmonds, E. A. Hajek, N. Downton, A. B. Bryk, Avulsion flow-path selection on rivers in foreland basins. *Geology* **44**, 695–698 (2016). doi:10.1130/G38082.1

39. D. J. Jerolmack, D. Mohrig, Conditions for branching in depositional rives. *Geology* **35**, 463–466 (2007). doi:10.1130/G23308A.1

40. M. Bryant, P. Falk, C. Paola, Experimental study of avulsion frequency and rate of deposition. *Geology* **23**, 365–368 (1995). doi:10.1130/0091-7613(1995)023<0365:ESOAFA>2.3.CO;2

41. J. P. M. Syvitski, G. R. Brakenridge, Causation and avoidance of catastrophic flooding along the Indus River, Pakistan. *GSA Today* **23**, 4–10 (2013). doi:10.1130/GSATG165A.1

42. J. Z. Pang, S. H. Si, Evolution of the Yellow River mouth: I. Historical shifts. *Oceonologia Limnol. Sin.* **10**, 136–141 (1979).

43. X. Chunting, Division and recognition of modern Yellow River delta lobes. *Geogr. Res.* **13**, 59–66 (1994).

44. H. Fan, H. Huang, T. Q. Zeng, K. Wang, River mouth bar formation, riverbed aggradation and channel migration in the modern Huanghe (Yellow) River delta, China. *Geomorphology* **74**, 124–136 (2006). doi:10.1016/j.geomorph.2005.08.015

45. S. Cohen, T. Wan, M. T. Islam, J. P. M. Syvitski, Global river slope: A new geospatial dataset and global-scale analysis. *J. Hydrol. (Amst.)* **563**, 1057–1067 (2018). doi:10.1016/j.jhydrol.2018.06.066

46. D. Yamazaki, S. Kanae, H. Kim, T. Oki, A physically based description of floodplain inundation dynamics in a global river routing model. *Water Resour. Res.* **47**, 2010WR009726 (2011). doi:10.1029/2010WR009726

47. S. M. Trampush, S. Huzurbazar, B. McElroy, Empirical assessment of theory for bankfull characteristics of alluvial channels. *Water Resour. Res.* **50**, 9211–9220 (2014). doi:10.1002/2014WR015597

48. J. H. Nienhuis, R. S. W. van de Wal, Projections of global delta land loss from sea-level rise in the 21st century *Geophys. Res. Lett.* **48**, e2021GL093368 (2021).

49. T. C. Ashley, B. McElroy, D. Buscombe, P. E. Grams, M. Kaplinski, Estimating bedload from suspended load and water discharge in sand bed rivers. *Water Resour. Res.*, **56**, e2019WR025883 (2020).

50. J. M. Turowski, D. Rickenmann, S. J. Dadson, The partitioning of the total sediment load of a river into suspended load and bedload: A review of empirical data. *Sedimentology* **57**, 1126–1146 (2010). doi:10.1111/j.1365-3091.2009.01140.x

51. H.-Y. Li, Z. Tan, H. Ma, Z. Zhu, G. W. Abeshu, S. Zhu, S. Cohen, T. Zhou, D. Xu, L. R. Leung, A new large-scale suspended sediment model and its application over the United States. *Hydrol. Earth Syst. Sci.* **26**, 665–688 (2022). doi:10.5194/hess-26-665-2022

52. M. P. Lamb, J. de Leeuw, W. W. Fischer, A. J. Moodie, J. G. Venditti, J. A. Nittrouer, D. Haught, G. Parker, Mud in rivers transported as flocculated and suspended bed material. *Nat. Geosci.* **13**, 566–570 (2020). doi:10.1038/s41561-020-0602-5

53. M. Manga, E. Brodsky, Seismic triggering of eruptions in the far field: Volcanoes and geysers. *Annu. Rev. Earth Planet. Sci.* **34**, 263–291 (2006). doi:10.1146/annurev.earth.34.031405.125125

54. M. Manga, C. Y. Wang, "Earthquake hydrology" in *Treatise on Geophysics*, G. Schubert, ed., (Elsevier, 2015), vol. 4, pp. 305–328

55. D. Montgomery, M. Manga, Streamflow and Water Well Responses to Earthquakes. *Science* **300**, 2047–2049 doi:0.1126/science.1082980 (2003).

56. A. J. Hartley, G. S. Weissmann, L. Scuderi, Controls on the apex location of large deltas. *J. Geol. Soc. London* **174**, 10–13 (2017). doi:10.1144/jgs2015-154